View metadata, citation and similar papers at core.ac.uk

brought to you by CORE

provided by Elsevier - Publisher Connector

Computer Physics Communications 185 (2014) 2221–2231

Contents lists available at ScienceDirect

Computer Physics Communications

journal homepage: www.elsevier.com/locate/cpc

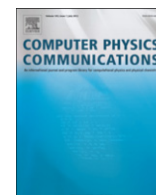

Ab initio calculation of the deformation potential and photoelastic coefficients of silicon with a non-uniform finite-difference solver based on the local density approximation

Jeremy Witzens *

Integrated Photonics Laboratory, RWTH Aachen, Sommerfeldstr. 24, 52074 Aachen, Germany

ARTICLE INFO

Article history:
Received 5 May 2013
Received in revised form
3 February 2014
Accepted 18 March 2014
Available online 25 March 2014

Keywords:
Deformation potential
Local density approximation
Finite-differences
Non-uniform meshing
Curvilinear coordinate transforms
Photoelastic tensor
Piezo-optical effect

ABSTRACT

The band diagram, deformation potential and photoelastic tensor of silicon are calculated self-consistently under uniaxial and shear strain by solving for the electronic wavefunctions with a finite-difference method. Many-body effects are accounted for by the local density approximation. In order to accommodate the large number of grid points required due to the diverging electrostatic potential near the atomic nuclei in an all-electron calculation, a non-uniform meshing is adopted. Internal displacements are taken into account by adding an additional coordinate transform to the method of Bir and Pikus. Good consistency of the calculated deformation potential and photoelastic coefficients is obtained with prior experimental and theoretical results, validating the numerical methods. Furthermore, it is shown that a slight correction of the multiplicative coefficient of the $X\alpha$ approximation for conduction bands results in good agreement with experiment for both the direct and indirect bandgaps.

© 2014 The Author. Published by Elsevier B.V.
This is an open access article under the CC BY-NC-ND license
(http://creativecommons.org/licenses/by-nc-nd/3.0/).

1. Introduction

Recent developments in electronics and optoelectronics have led to a rekindled interest in the modeling of strained semiconductors. The best known device application is the improvement of carrier mobility in strained silicon that has allowed further scaling of Moore's law [1]. Strained semiconductors are also of great interest to photonics and optoelectronics: For example, applying strain to quantum wells is a well known technique to improve the performance of semiconductor lasers [2]. More recently, strained group IV semiconductors have gained in importance for the CMOS compatible fabrication of photonic circuits (Silicon Photonics [3]). Inhomogeneously strained silicon has been shown to have a finite second order optical nonlinearity enabling photonic devices such as silicon based Pockels modulators and two photon converters [4,5]. Highly n-doped germanium has been shown to support optical gain [6]. Further narrowing of the direct bandgap via tensile strain could further improve the material's gain and enable more efficient group IV light sources [7,8]. The SiGeSn material system allows the realization of highly strained germanium and GeSn quantum wells [9] and might pave the way towards practical devices.

We solve the Kohn–Sham equation [10] for strained cubic semiconductors with a finite-difference (FD) real-space all-electron approach and apply it to the case of strained silicon. In order to assess the method's suitability to the determination of the optical properties of strained semiconductors, we carefully benchmark it by calculating the deformation potential and the photoelastic coefficients of silicon under uniaxial and shear strain.

All-electron modeling can lead to more accurate results in problems that involve a high level of interaction between valence and lower orbital electrons [11,12], certain classes of problems that require treatment of lower orbitals [13,14], or the determination of absolute energies [15] and absolute deformation potentials [16] referenced against energy levels of lower orbitals. Our interest is to apply all-electron treatment to the modeling of novel effects such as the Pockels effect in inhomogeneously strained silicon for which pseudopotentials have not yet been carefully benchmarked. However, treatment of the diverging electrostatic potential around the nucleus and rapid oscillations of the wavefunctions in its vicinity result in a multi-scale numerical problem [17] that needs to be addressed, e.g., with hierarchical finite elements bases [18,19] or real-space methods with grid refinements around the nucleus [20–24]. Real-space finite-difference methods have the general advantage of resulting in sparse matrices with a small number of off-diagonal

* Tel.: +49 2418020021; fax: +49 2418022212.
E-mail address: jwitzens@iph.rwth-aachen.de.

http://dx.doi.org/10.1016/j.cpc.2014.03.016
0010-4655/© 2014 The Author. Published by Elsevier B.V. This is an open access article under the CC BY-NC-ND license (http://creativecommons.org/licenses/by-nc-nd/3.0/).

terms, which can be efficiently diagonalized with parallel computing algorithms.

A number of methods have been demonstrated to adapt FD algorithms to handle the diverging potential of the nucleus. In [20,21], a rectangular cartesian grid was successively refined in concentric regions around the nucleus. In [20], orphan nodes were handled by generalizing the finite-difference expression of the Laplacian. In [21] the multi-grid problem was solved based on a V-cycle. In [22,23], a regular grid was used after applying a curvilinear spatial transformation, effectively increasing the number of grid points around the nucleus in the original coordinate system. In [24], the wavefunction was solved on a coarse rectangular grid and subsequently interpolated on a fine grid around the nuclei prior to calculating overlap integrals with pseudopotentials. Finally, in [25] the wavefunctions were solved for on a coarse grid excluding the space regions within a muffin-tin radius in the immediate vicinity of the nuclei. These excluded regions were handled by applying a boundary condition to the grid points closest to the nuclei forcing the wavefunctions on the boundary to be a superposition of atomic-like solutions. Here, we apply successive cartesian grid refinements to concentric regions centered on the nuclei, similarly to [20,21], and extend the methodology to calculate the band diagram and dielectric constant of strained semiconductors. The nested grid refinements used here allow more straight forward control over the extent and range of the grid refinements relative to methods based on curvilinear transformations [17,23], but require special handling of the derivative operators at the subgrid boundaries [20]. Here, we express the numerical problem as a sparse matrix diagonalization that can be straightforwardly handled with the Lanczos algorithm implemented in standard numerical packages.

The deformation of the crystal lattice is handled by a curvilinear coordinate transform that maps the strained onto the unstrained lattice. This allows, e.g., for the computation of the effect of internal strain with finite differences without numerical artifacts resulting from displacements of the nuclei relative to the grid points and generally for a smooth treatment of the effect of strain. The coordinate system is deformed in order for individual nuclei to remain on the same grid points irrespectively of the lattice deformation. In addition to the deformation introduced by Bir and Pikus [26,27], an additional curvilinear coordinate transform is introduced in order to accommodate internal displacements inside the unit cell [28].

Many-body effects are accounted for by using the $X\alpha$ approximation [10,29,30] in the framework of density functional theory [31] (DFT) and of the local density approximation (LDA). While the electrostatic and LDA potentials of inner shell electrons are fully taken into account, the shape of the inner orbitals are assumed to correspond to that of isolated silicon atoms (frozen core, all-electron approximation (FCAE)). While the numerical methods described here could easily be extended to the treatment of inner shell electrons, the frozen core approximation is adequate for the numerical studies reported here and is adopted to shorten computation time. The numerical methods used here could also be applied to other semiconductors or to materials of arbitrary shape following the path shown in [21], thus providing high flexibility for the modeling of irregular shapes.

In order to validate the numerical methods, we calculate the strained band diagram, the deformation potential and the photoelastic coefficients of silicon under uniaxial and shear strain. Convergence and accuracy, as well as required computational resources are carefully benchmarked. The deformation potential is derived both directly and in the framework of perturbation theory with a linearized perturbation Hamiltonian. Numerical results for the deformation potential and the photoelastic coefficients of strained silicon are compared to the literature, with good agreement. Furthermore, in order to determine the primary factors affecting the deformation potential, the overall deformation potential is broken down in the framework of a perturbation theoretical approach into individual contributions from the LDA potential, nuclei induced dipoles, dipoles induced by valence electrons, electrostatic potential due to redistribution of the valence electron density and screening from inner shells.

2. Coordinate transformation

Given a strain ϵ_{ij}, the method of Bir and Pikus starts by introducing the transformation

$$x'_i = x_i + \sum_{j=1..3} \epsilon_{ij} x_j \tag{1}$$

where x'_i corresponds to the physical coordinates of the strained unit cell that are mapped to a new coordinate system x_i. The latter corresponds to the unstrained unit cell, in that nuclei are located at their original position. There are two atoms in the unit cell of crystalline silicon. When shear strain is applied, in addition to the overall deformation of the unit cell, the two silicon atoms undergo an internal displacement relative to one another [28,32] parameterized by a number typically denoted as ζ. When a shear strain is applied to the unit cell, the lengths of the atomic bonds between adjacent nuclei become unequal, subdividing them into two categories. This can be fully or partially compensated by the internal displacement. $\zeta = 0$ corresponds to a total absence of internal displacement, i.e., the displacement of both atoms is predicted by Eq. (1). $\zeta = 1$ corresponds to a full equalization of the bond lengths. The unit cell considered here has dimensions $[a/2, a/2, a]$, where a is the lattice constant of silicon, with atoms placed at (1a) $[0, 0, 0]$, (1b) $[a/2, a/2, 0]$, (1c) $[0, 0, a]$, (1d) $[a/2, a/2, a]$ (each split between 8 unit cells), (1e) $[a/2, 0, a/2]$, (1f) $[0, a/2, a/2]$ (each split between 4 unit cells) and a second atom placed at (2) $[a/4, a/4, a/4]$. Atom (2) is connected with sp3 bonds to (1a), (1b), (1e) and (1f). For a shear strain ϵ_{ij}, the second atom (2) is displaced by $\delta x_k = -\zeta \epsilon_{ij} a/2$ relative to atoms of the first category (1a–1f), where $i \neq j \neq k$.

In order to accommodate the internal displacement without creating numerical artifacts in the finite-difference solver resulting from a displacement of the nuclei relative to the grid, we introduce an additional term in the coordinate transform

$$x'_i = x_i + \sum_{j=1..3} \epsilon_{ij} x_j - \sum_{i \neq j} \frac{\delta x_i}{4} \cos\left(\frac{4\pi x_j}{a}\right) \tag{2}$$

$$x'_i = x_i + \sum_{j=1..3} \epsilon_{ij} x_j + \frac{\zeta a}{8} \sum_{i \neq j \neq k} \epsilon_{jk} \cos\left(\frac{4\pi x_j}{a}\right). \tag{3}$$

This transformation maps the position of the nuclei in the unstrained unit cell to the position of the nuclei in the strained unit cell. Since the Hamiltonian will be described in the coordinate system of the unstrained lattice, x_i, rather than in the physical coordinate system of the strained lattice, x'_i, this results in a description of the problem where the nuclei are always located on the same grid points, irrespectively of the strain that is applied to the lattice and irrespectively of ζ.

The Laplace operator of the physical coordinate system can be expressed in the unstrained coordinates as

$$\begin{aligned} \Delta' = {} & \Delta - 2 \sum_{i,j=1...3} \epsilon_{ij} \frac{\partial^2}{\partial x_i \partial x_j} \\ & - \frac{2\pi}{a} \sum_{i \neq j} \delta x_i \sin\left(\frac{4\pi}{a} x_j\right) \frac{\partial^2}{\partial x_i \partial x_j} \\ & - \frac{4\pi^2}{a^2} \sum_{i \neq j} \delta x_i \cos\left(\frac{4\pi}{a} x_j\right) \frac{\partial}{\partial x_i} \end{aligned} \tag{4}$$

$$\Delta' = \Delta - 2\sum_{i,j=1\ldots3}\epsilon_{ij}\frac{\partial^2}{\partial x_i\partial x_j} + \pi\zeta\sum_{i\neq j\neq k}\epsilon_{jk}\sin\left(\frac{4\pi}{a}x_j\right)\frac{\partial^2}{\partial x_i\partial x_j} + \frac{2\pi^2\zeta}{a}\sum_{i\neq j\neq k}\epsilon_{jk}\cos\left(\frac{4\pi}{a}x_j\right)\frac{\partial}{\partial x_i}. \quad (5)$$

The perturbation Hamiltonian can then be written as

$$\delta H = \frac{\hbar^2}{m}\sum_{i,j=1\ldots3}\epsilon_{ij}\frac{\partial^2}{\partial x_i\partial x_j} - \frac{\hbar^2}{2m}\pi\zeta\sum_{i\neq j\neq k}\epsilon_{jk}\sin\left(\frac{4\pi}{a}x_j\right)\frac{\partial^2}{\partial x_i\partial x_j} - \frac{\hbar^2}{m}\frac{\pi^2\zeta}{a}\sum_{i\neq j\neq k}\epsilon_{jk}\cos\left(\frac{4\pi}{a}x_j\right)\frac{\partial}{\partial x_i} - e\delta V \quad (6)$$

where m is the mass of the electron and e is the elementary electric charge. $\delta V = V' - V$, where V' and V are respectively the sum of the electrostatic and LDA potentials in the strained (V') and unstrained (V) lattice.

3. Grid definition and differential operators

The unrefined grid consists in a rectangular grid with vertices spaced by $a/32$, i.e., with 8192 vertices in the unit cell. This grid is successively refined inside cubes centered on the nuclei (Fig. 1). For a nucleus located at (x_0, y_0, z_0), we denote $\delta = max(|x - x_0|, |y - y_0|, |z - z_0|)$. For $\delta \le a/512$, $\delta \le 3a/512$, $\delta \le a/64$, $\delta \le a/32$, $\delta \le a/16$ and $\delta \le 3a/32$ the grid size is respectively $a/2048$, $a/1024$, $a/512$, $a/256$, $a/128$ and $a/64$ (the grid refinements were first evaluated and optimized on a simpler 1D problem consisting in verifying the accuracy of higher orbital energies of isolated silicon atoms). This results in a total of 41 920 vertices, about 5 times the number of points of the unrefined grid. Even though this is a very large number of vertices, the eigensolutions can still be calculated in a short time with a desktop computer [33] using the Lanczos algorithm [34] since the Laplace operator results in a sparse matrix.

At the boundary between a refined and a coarser grid, hanging nodes are missing one or two nearest neighbors. As a first step to derive the differential operators, these nearest neighbors are interpolated so as to subsequently allow the numerical evaluation of the differential operators (in practice the numerical problem reduces to the diagonalization of a matrix resulting from the product of an interpolation and a finite-difference operator). In Fig. 2(a), the wavefunction is interpolated at points 11 and 14 as

$$\psi(p_{11}) = \psi(p_2) + \frac{1}{2}\left(\psi(p_{10}) + \psi(p_{12}) - \psi(p_1) - \psi(p_3)\right) \quad (7)$$

$$\psi(p_{14}) = \psi(p_5) + \frac{1}{4}\left(\psi(p_{10}) + \psi(p_{12}) + \psi(p_{16}) + \psi(p_{18}) - \psi(p_1) - \psi(p_3) - \psi(p_7) - \psi(p_9)\right). \quad (8)$$

Points 13, 15 and 17 are interpolated in a similar manner to 11. The three terms of the Laplace operator are evaluated at a point p_0 as

$$\frac{\partial^2}{\partial x^2}\psi = \frac{2\delta_{x-}\psi(p_{x+}) + 2\delta_{x+}\psi(p_{x-}) - 2(\delta_{x-} + \delta_{x+})\psi(p_0)}{\delta_{x+}^2\delta_{x-} + \delta_{x+}\delta_{x-}^2} \quad (9)$$

where p_{x-} is the grid point immediately to the left of p_0, p_{x+} is the point immediately to the right, δ_{x-} is the distance between p_{x-} and p_0, and δ_{x+} is the distance between p_0 and p_{x+}. The single derivatives are calculated as

$$\frac{\partial}{\partial x}\psi = \frac{\delta_{x-}^2\psi(p_{x+}) - \delta_{x+}^2\psi(p_{x-}) - \left(\delta_{x-}^2 - \delta_{x+}^2\right)\psi(p_0)}{\delta_{x+}^2\delta_{x-} + \delta_{x+}\delta_{x-}^2}. \quad (10)$$

The lattice vectors of silicon are given by $v_1 = (a/2, 0, a/2)$, $v_2 = (0, a/2, a/2)$ and $v_3 = (a/2, a/2, 0)$. Since $(0, 0, a) = v_1 + v_2 - v_3$, the points at $z = 0$ and at $z = a$ are related by the relation $\psi(x, y, a) = \psi(x, y, 0)\cdot e^{ik_z a}$, where $k = (k_x, k_y, k_z)$ is the reduced wave-vector of the Bloch-mode. Similarly, $\psi(a/2, y, z + a/2) = \psi(0, y, z)\cdot e^{ik_x a/2 + ik_z a/2}$ for $z \le a/2$ and $\psi(a/2, y, z - a/2) = \psi(0, y, z)\cdot e^{ik_x a/2 - ik_z a/2}$ for $z > a/2$ (equivalent relations relate the boundaries at $y = 0$ and $y = a/2$). These relations are taken into account to evaluate the derivative operators at the unit cell boundaries, thus taking into account the periodic boundary conditions of the eigenvalue problem.

4. Electrostatic potential and LDA correction

Many-body effects are taken into account with the local density approximation by adding Slater's exchange energy [29] to the electrostatic energy with a corrective factor α ($X\alpha$ approximation). Correlation effects [36] are much weaker than the exchange term [30] and are not *explicitly* taken into account. The exchange energy is given by

$$-eV_x = -\alpha\frac{e^2}{4\pi\varepsilon_0}\frac{3}{2}\left(\frac{3}{\pi}\left(\rho + \sum_k \rho_{in}(r_k)\right)\right)^{\frac{1}{3}} \quad (11)$$

where ρ is the electron density of the valence electrons, ρ_{in} is the electron density of the inner orbitals for a single atom centered on the kth nucleus, r_k is the distance to the kth nucleus, and α is a parameter used to adjust the strength of the exchange potential. The parameter α was derived to be $2/3$ by Kohn and Sham [10] in the framework of DFT.

Eq. (11) is based on the exchange energy of the free electron gas. This exchange energy, as derived from the Hartree–Fock method, is dependent on the electron wave-vector with a proportionality constant given by

$$\alpha = \frac{4}{3}\left(\frac{1}{2} + \frac{1-\eta^2}{4\eta}\ln\left(\frac{1+\eta}{1-\eta}\right)\right) \quad (12)$$

where $\eta = k/k_F$ is the ratio between the free electron wave-vector and the wave-vector at the Fermi level. This is a monotonically decreasing function equal to $4/3$ at $\eta = 0$, to $2/3$ at $\eta = 1$ and decaying to zero at large η. In the original derivation by Slater [29], the exchange energy was averaged over all wave-vectors up to the Fermi level, resulting in $\alpha = 1$. In the subsequent derivation by Kohn and Sham [10] done in the framework of DFT, α was derived as $2/3$ and corresponds to the value of Eq. (12) at the Fermi level.

Since $\alpha = 2/3$ results in smaller bandgaps than in experiment, it has been suggested [30] to adjust α empirically in order to recover the experimental bandgap. It was shown that increasing α leads to a larger indirect bandgap resulting from a flattening of the bands. However, as also pointed out in [30], this is not fully satisfactory, since the discrepancy between theory and experiment remains essentially unchanged for the direct bandgap. Since the coefficient given by Eq. (12) is decreasing with η and since the wavefunctions of the conduction bands generally have a higher frequency content than the wavefunctions of the valence bands, it seems a natural correction to assume a lower α for the conduction bands than for the valence bands. This strictly breaks the framework of LDA, since the LDA potential is now dependent on the electronic band. As shown in Fig. 2(b), this results however in a very good agreement between the calculated band diagram and a more

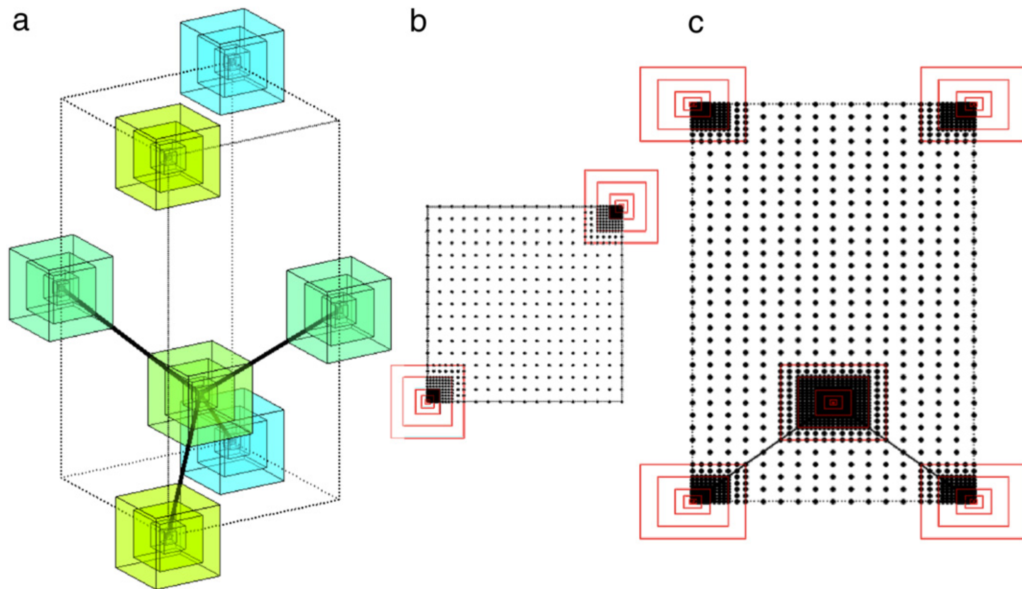

Fig. 1. Illustration of the grid refinements. (a) shows a unit cell. The thick lines represent silicon–silicon bonds. The cubes represent regions of space in which the grid is being successively refined. (b) shows the grid along a cross-section on the (0 0 1) plane passing through the origin. Regions of successive grid refinement are represented by red squares. (c) shows the grid along the cross-section along the (1–1 0) plane passing through the origin.

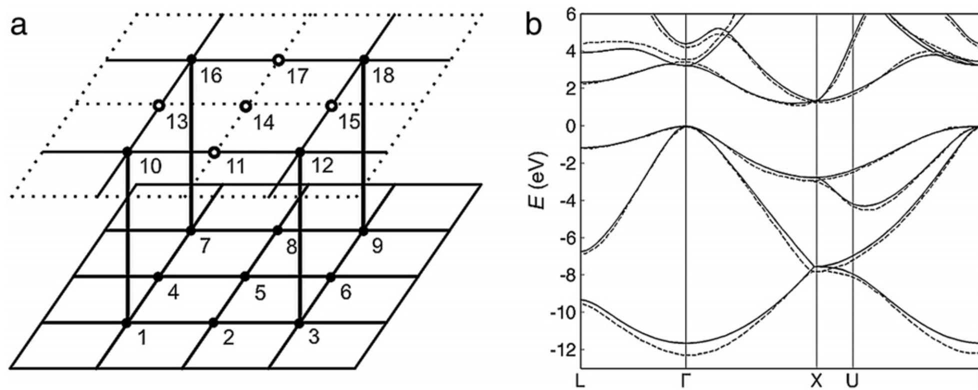

Fig. 2. (a) Illustration of hanging nodes and interpolated nodes (unfilled circles) at the boundary to a coarser grid. The numbering is used to describe the interpolation procedure in the text. (b) Comparison between the band diagram calculated with adjusted $X\alpha$ coefficient (continuous line) and a band diagram calculated with non-local empirical pseudopotentials.
Source: Adapted from Ref. [35].

accurate band diagram calculated with a non-local empirical pseudopotential method in close agreement with experiment [35]. The varying α can be justified both because the DFT theorem has only been proven for the ground state of the system, i.e., for the valence bands, and because LDA itself is an approximation that only partially reflects the true kernel of the non-local DFT potential.

Fig. 2(b) shows the band diagram of silicon computed with LDA, where the coefficient α has been reduced by 1/24th for the conduction band (N_t as defined in Section 4.1 is equal to 6 and $\alpha = 5/6$ for the valence band). The corresponding weakening of the conduction band exchange energy and the resulting increase in conduction band energy are sufficient to obtain good consistency for both the direct and the indirect bandgaps. The calculated indirect bandgap is 1.18 eV (versus 1.17 eV measured at 0 K [37]) and the calculated direct bandgap between the upper valence band and the fourth conduction band ($\Gamma'_{25v} \rightarrow \Gamma'_{2c}$) is 4.30 eV (versus 4.18 eV measured at 4.2 K [38]).

4.1. Potential

The potential is calculated as the combination of the electrostatic potentials of the nuclei and of the electron distribution with the exchange potential given by Eq. (11). Rather than obtaining the electrostatic potential by solving the Laplace equation, it is obtained by summing up individual contributions of the nuclei and electrons. While being a less computationally efficient method for periodic problems with a potential following a well known differential equation, it facilitates the extension of the method to aperiodic systems or to more general potentials. In particular, it is adapted here to the perturbative potential generated by a homogeneous lattice deformation and can be readily generalized to the perturbative potential generated by an inhomogeneous lattice deformation or other general potentials with a well known Green's function. The potential is calculated in the framework of the frozen core, all-electron approximation (FCAE), i.e., the electrostatic potentials and LDA correction of inner shell electrons are taken into account, but inner electrons are assumed to correspond to orbitals of isolated silicon atoms.

Spatially varying screening of the nuclei takes into account the electrostatic potential of inner electron shells. In order to compute the contribution of the valence electron density distribution to the electrostatic potential, the latter is approximated by a series of point charges distributed on a coarse grid with a grid size $a/32$ that is offset by $(a/64, a/64, a/64)$ relative to the grid on which the

wavefunction is calculated. While the kinetic term of the Hamiltonian and the electrostatic potential of the nuclei are computed on the refined grid, for the purpose of calculating the distance to the distributed electrons and deriving the electrostatic potential associated to the electron density distribution, the wavefunction grid is also snapped to its coarsest mesh ($a/32$). This ensures that no diverging terms occur, since the two grids are offset relative to each other and have no common vertices. Similarly, in order to truncate the divergence of the electrostatic potential created by the nuclei, distances to the nuclei smaller then 1/2 the finest grid size (smaller than $a/4096$) are rounded up to $a/4096$ (this applies to the points where the nuclei are located). In order to calculate the electrostatic potential with a finite sum over nuclei and distributed electron point charges, the infinite reach of the unscreened Coulomb potential is truncated by progressively ramping it down for radii larger than $N_t \cdot a/2$ and forcing it to zero for radii above $(N_t + 4) \cdot a/2$. In the following, results are reported for $N_t = 6$.

The calculation of the electrostatic potential generated by the valence electron density distribution is a computationally intensive process. In order to accelerate the calculation, the grid-point to grid-point contributions are only directly taken into account for the electron density in a volume of 75 unit cells surrounding the computational domain. Farther electrons are taken into account by a multipole expansion of the electrostatic potential created by the unit cell, with a Taylor expansion of the generated potential to the third polynomial order (i.e., with terms scaling as $\delta x^{i1} \delta y^{i2} \delta z^{i3}$, where $(\delta x, \delta y, \delta z)$ is the displacement between the point where the electrostatic potential is applied and the center of the unit cell acting as the source of the potential and where $i1$, $i2$ and $i3$ are integers such that $i1 + i2 + i3 \leq 3$).

4.2. Perturbative potential

The perturbative potential $V' - V$ can be directly obtained by replacing each of the charges by an electrostatic dipole whose strength depends on the distance to the point at which the field is calculated, thus effectively linearizing the perturbation Hamiltonian as a function of strain. This method can be readily extended to aperiodic problems of a more general nature. Additional terms take into account modified screening of the nuclei, as well as the redistribution of the valence electron density distribution. The perturbative term arising from the LDA potential is derived by linearizing the strain induced changes of the local electron density.

Given a strain tensor $\bar{\bar{\epsilon}}$, the strain induced displacement of a nucleus initially located at (x_0, y_0, z_0) relative to a point initially located at (x_p, y_p, z_p) is given by $\delta x_i = \epsilon_{ij}(x_{0j} - x_{pj}) + \frac{\zeta a}{8} \sum_{i \neq j \neq k} \epsilon_{jk} (\cos(\frac{4\pi}{a} x_{0j}) - \cos(\frac{4\pi}{a} x_{pj}))$. This gives rise to a dipole of magnitude $\vec{d} = q\delta x_i$ and to an electrostatic potential

$$\begin{aligned} \delta V_1(p) = &-\frac{Ze}{4\pi\varepsilon_0} \left(\sum_i \left(x_{0i} - x_{pi}\right)^2 \right)^{-\frac{3}{2}} \\ &\times \left(\sum_{i,j} \epsilon_{ij} \left(x_{0j} - x_{pj}\right) \left(x_{0i} - x_{pi}\right) + \frac{\zeta a}{8} \sum_{i \neq j \neq k} \epsilon_{jk} \left(\cos\left(\frac{4\pi}{a} x_{0j}\right) \right.\right. \\ &\left.\left. - \cos\left(\frac{4\pi}{a} x_{pj}\right)\right) \left(x_{0i} - x_{pi}\right) \right) \end{aligned} \tag{13}$$

where $q = Ze$ is the charge of the nucleus and ε_0 is the permittivity of free space. For hydrostatic strain $\bar{\bar{\epsilon}} = \epsilon \cdot Id$, where Id is the 3×3 identity matrix, this expression takes the simple form of an additional electrostatic potential directly opposed to the unperturbed one

$$\delta V_1(p) = -\frac{Ze}{4\pi\varepsilon_0} \frac{\sum_i \epsilon \left(x_{0i} - x_{pi}\right)^2}{\left(\sum_i \left(x_{0i} - x_{pi}\right)^2\right)^{\frac{3}{2}}} = -\frac{Ze\epsilon}{4\pi\epsilon_0} \frac{1}{r} \tag{14}$$

where r is the distance between the nucleus and the point where the field is calculated.

A second perturbative term arises from the redistribution of the electron density distribution. The inner shells are assumed to simply shift with the position of the nucleus to which they are bound and can be taken into account by adjusting the screening of the nucleus

$$\delta V_2(p) = \frac{e}{4\pi\varepsilon_0 r} \frac{dZ(r)}{dr} \delta r \tag{15}$$

$$\begin{aligned} = &\frac{e}{4\pi\varepsilon_0 r^2} \frac{dZ(r)}{dr} \left(\sum_{i,j} \epsilon_{ij} \left(x_{0j} - x_{pj}\right) \left(x_{0i} - x_{pi}\right) \right. \\ &+ \frac{\zeta a}{8} \sum_{i \neq j \neq k} \epsilon_{jk} \left(\cos\left(\frac{4\pi}{a} x_{0j}\right) \right. \\ &\left.\left. - \cos\left(\frac{4\pi}{a} x_{pj}\right)\right) \left(x_{0i} - x_{pi}\right) \right). \end{aligned} \tag{16}$$

Here too, Eq. (16) takes a simplified form in the case of hydrostatic strain

$$\delta V_2(p) = \frac{e\epsilon}{4\pi\varepsilon_0} \frac{dZ(r)}{dr} \tag{17}$$

where it should be noted that dZ/dr is a rapidly decaying negative function (the screened charge is constant and equal to $4e$ far from the nucleus).

The valence electron distribution in the strained unit cell (ρ') can be described as a function of the unstrained or the strained lattice coordinates, with corresponding normalizations given by

$$\int \rho'\left(x'\right) d^3x' = 8 \tag{18}$$

$$\int \rho'\left(x'(x)\right)\left(1 + tr\left(\bar{\bar{\epsilon}}\right)\right) d^3x = 8. \tag{19}$$

We introduce $\hat{\rho}(x) = \rho'(x'(x))(1 + tr(\bar{\bar{\epsilon}}))$. This corresponds to the redistributed valence electron density described in the coordinate system and the normalization of the undistorted silicon lattice. If we note the volume element of the *undistorted* lattice as $dv = d^3x$, the redistribution of the electron density function is taken into account by

$$\delta V_3(p) = -\frac{edv}{4\pi\varepsilon_0 r} \left(\hat{\rho}(x) - \rho(x)\right) \tag{20}$$

$$= -\frac{edv}{4\pi\varepsilon_0 r} \frac{\partial \hat{\rho}(x)}{\partial \epsilon_{ij}} \epsilon_{ij}. \tag{21}$$

The displacement of the electron density distribution due to the lattice deformation is taken into account by a potential δV_4 that takes the same form as Eq. (13).

Finally the variation of the exchange *energy* is taken into account by

$$\begin{aligned} -e\delta V_5(p) = &-\alpha \frac{e^2}{8\pi\varepsilon_0} \left(\frac{3}{\pi}\right)^{\frac{1}{3}} \left(\rho + \sum_k \rho_{in}(r_k)\right)^{-\frac{2}{3}} \\ &\times \left(\frac{\partial \hat{\rho}(x)}{\partial \epsilon_{ij}} \epsilon_{ij} - \hat{\rho}(x)\, tr\left(\bar{\bar{\epsilon}}\right) + \sum_{i,j,k} \frac{\partial \rho_{in}(r_k)}{\partial r} \frac{\epsilon_{ij}\left(x_{kj} - x_{pj}\right)\left(x_{ki} - x_{pi}\right)}{r_k} \right. \\ &\left. + \frac{\zeta a}{8} \sum_{i \neq j \neq l,k} \frac{\partial \rho_{in}(r_k)}{\partial r} \frac{\epsilon_{jl}\left(\cos\left(\frac{4\pi}{a} x_{kj}\right) - \cos\left(\frac{4\pi}{a} x_{pj}\right)\right)\left(x_{ki} - x_{pi}\right)}{r_k} \right) \end{aligned} \tag{22}$$

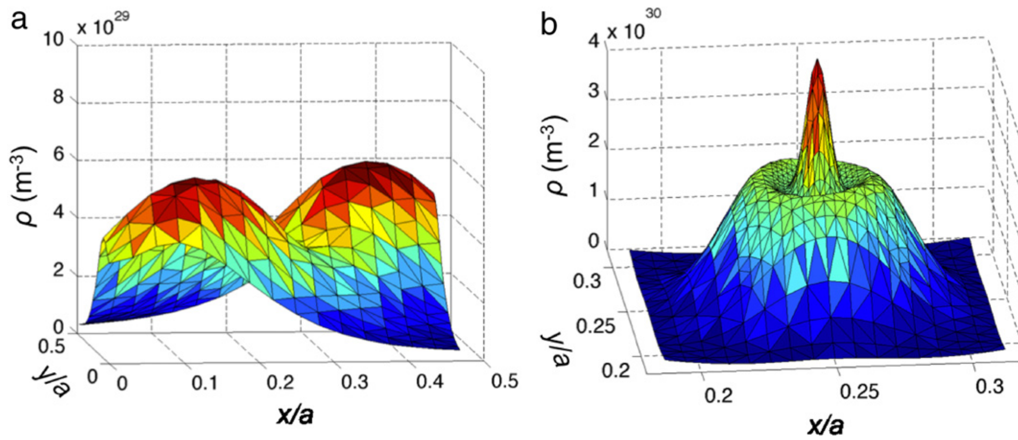

Fig. 3. Self-consistent electron density distribution at $z = a/8$ and on the refined grid close to the nucleus of atom (2) at $z = a/4 - a/128$.

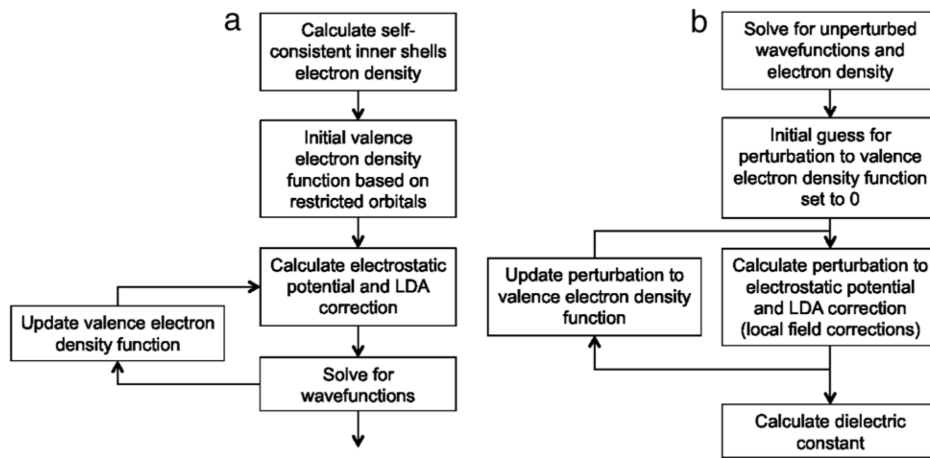

Fig. 4. (a) Flow of the wavefunction and band energy computation and (b) flow of the dielectric constant computation. The term "perturbed" in (b) refers to perturbed by the external electric field. Inclusion of lattice strain is implicit in both diagrams.

where r_k and x_k are respectively the distance to and the position of the kth nucleus. The first term in the bottom parenthesis corresponds to the redistribution of the valence electrons, the second term to the modification of the valence electron density due to the volume element change. The third and fourth terms arise from the displacement of the inner core electrons tracking the displacement of the nuclei to which they are bound.

5. Self-consistent electron density distribution

The self-consistent valence electron density distribution is iteratively calculated. The initial guess is obtained by adding the electron densities of sp3 bonds calculated in the strained lattice with restricted orbitals [39,40]. The specific orbital restriction parameters are taken from an unpublished tight binding study in which they were optimized in view of getting a good agreement between the physical band diagram and the band energies back-calculated from the wavefunctions obtained with the third nearest neighbor tight binding coefficients published in [41]. We opt for an implicit orbital confinement [42]. The restricted orbital ψ_r is obtained from the unrestricted orbital ψ via the transformation $\psi_r(r) = \psi(r')$, where r' is obtained from r via a transformation parameterized by two radii r_1 (at which the restriction starts having an effect) and r_2 (the radius within which the orbital is fully confined). For $r \le r_1$, $r = r'$. For $r > r_1$ the transformation is given by

$$r' = r_1 + \frac{r - r_1}{1 - \frac{r-r_1}{r_2-r_1}}. \tag{23}$$

For r approaching r_2, $r' \to \infty$ so that the orbitals are restricted to a maximum radius of r_2. Parameter values $r_1 = 2.9a_0$ and $r_2 = 4.9a_0$ were used, where a_0 is the Bohr radius. As can be seen in the section on algorithmic convergence, this yields a reasonable initial estimate and the self-consistent electron density function converges to a high degree within five iterations.

In order to refine the electron density distribution, at each iteration wavefunctions for half the Brillouin cell are calculated, with regularly spaced reduced wave-vectors located on a grid with $\Delta k = 0.4\pi/a$. Since homogeneous strain does not break the centrosymmetry of silicon, the rest of the Brillouin zone can be obtained by simple symmetry considerations resulting in an effective total of 424 k-space points. The squares of the wavefunctions are then summed over the entire Brillouin zone in order to obtain the electron density. As a final step, the electron density is normalized to yield a total of 8 valence electrons in the unit cell. This process is repeated iteratively in order to obtain the self-consistent electron density. Fig. 3 shows the electron density function at two cross-sections through the unit cell with a smooth distribution even very close to the nucleus. The overall computation flow is summarized in Fig. 4(a).

6. Numerical results for the deformation potential

This section summarizes the numerical results, including convergence of the self-consistent electron distribution, a comparison of the calculated deformation potential with literature values, as well as a detailed look at the influence of individual perturbative

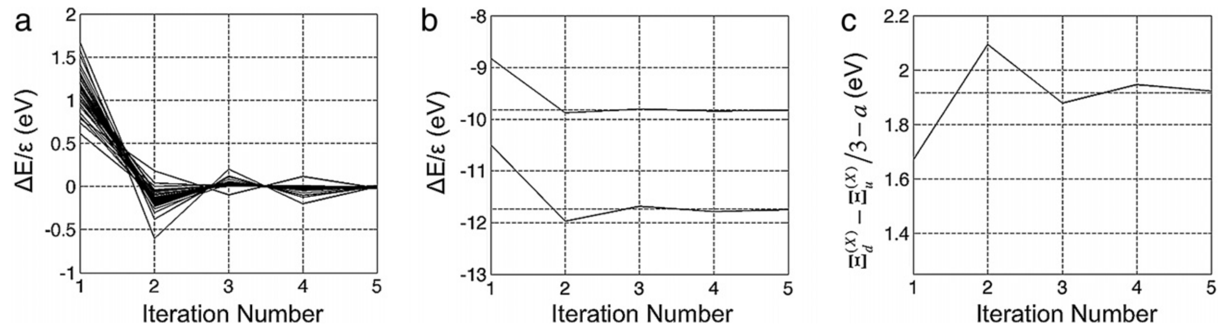

Fig. 5. Convergence of the calculated deformation potentials as a function of the number of iterations. (a) shows the calculated energy level shifts for the 4 valence and first 4 conduction bands for all high-symmetry points under the influence of a uniaxial strain of magnitude ϵ along the [001] axis. The average value over iteration numbers 3–5 has been subtracted in order to visualize the convergence and overlay the plots. (b) shows the same data for the Δ point of the first conduction band (upper curve) and for the Γ point averaged over the three upper valence bands (lower curve). The dashed curves show the averages over iteration numbers 3–5. (c) shows the extracted deformation potential as a function of the iteration number, as well as the average over iteration numbers 3–5 (dashed curve). All calculations were made with $N_t = 6$ and $\alpha = 5/6$.

Table 1
Comparison of calculated deformation potential coefficients with literature values (in eV).

Coefficient	Calculated value	Lit. experimental	Lit. theory
$\Xi_u^{(\Delta)}$	8.94[a], 8.89[b]	8.1 ± 0.3[c], 8.77 ± 0.07[d], 8.6 ± 0.4[e], 9.0 ± 0.4[f], 8.6 ± 0.2[g], 9.2 ± 0.3[h]	10.5[k], 9.29[l], 8.47[m], 9.16[n]
$\Xi_u^{(L)}$	15.19[a], 15.02[b]		18[k], 12.35[m], 16.14[n]
$\Xi_d^{(\Delta)} + \Xi_u^{(\Delta)}/3 - a$	1.73[a], 1.50[b]	1.6 ± 0.3[c], 1.5 ± 0.3[e], 3.8 ± 0.5[g], 3.1 ± 0.5[h]	2.5[k], 0.29[l], 1.79[m], 1.72[n]
$\Xi_d^{(X)} + \Xi_u^{(X)}/3 - a$	1.92[a], 1.69[b]		1.84[i], 1.35[j]
$\Xi_d^{(L)} + \Xi_u^{(L)}/3 - a$	−3.52[a], −3.76[b]		−3.60[i], −4.07[j], −3.1[k], −3.65[l], −2.84[m], −3.12[n]
$a^{\Gamma-\Gamma}$	−11.50[a], −11.75[b]		−11.39[i], −12.44[j], −12.3[o], −11.84[p]

[a] Calculated with $\alpha = 5/6$ for both valence and conduction bands.
[b] Calculated with $\alpha = 5/6$ for the valence bands and $\alpha = 5/6 \times 23/24$ for the conduction bands.
[c] Ref. [47], Experimental (Stress dependence of excitons), $T = 77$ K (1978).
[d] Ref. [46], Experimental (Piezospectroscopy of donors), $T = 4$ K (1972).
[e] Ref. [45], Experimental (Exciton Energy), $T = 77$ K (1971).
[f] Ref. [44], Experimental (Cyclotron Resonance), $T = 4.2$ K (1970).
[g] Ref. [43], Experimental (Exciton Energy/Absorption Spectroscopy), $T = 80$ K (1966).
[h] Ref. [43], Experimental (Exciton Energy/Absorption Spectroscopy), $T = 295$ K (1966).
[i] Ref. [53], Linearized Augmented Plane-Wave Method with LDA approximation (1999).
[j] Ref. [53], Linearized Augmented Plane-Wave Method with LDA approximation and correction based on external potential (1999).
[k] Ref. [52], Empirical Pseudopotential, $\zeta = 0.53$ (1996).
[l] Ref. [51], Empirical Pseudopotential (1993).
[m] Ref. [50], Empirical Pseudopotential, $\zeta = 0.53$ (1989).
[n] Ref. [49], Pseudopotential with LDA approximation, $\zeta = 0.53$ (1986).
[o] Ref. [55], Tight Binding (1995).
[p] Ref. [54], Tight Binding (1993).

terms and of the internal displacement parameter ζ on the deformation potential.

6.1. Convergence study

Fig. 5 shows the convergence of the solver with the number of iterations applied to obtain the self-consistent electron distribution. It can be seen that the calculated deformation potentials converge quickly and are almost fully converged after 5 iterations.

6.2. Comparison to the literature

Table 1 shows a comparison of the calculated deformation potentials (5 iterations, $N_t = 6, \alpha = 5/6$) with literature [43–55]. ζ is assumed to be 0.53 as is also the case in [49,50,52,56] and in close agreement with measured values [57]. Good agreement of the calculated deformation potentials can be seen with previously determined values, validating the numerical methods. $a^{\Gamma-\Gamma}$ refers to the deformation potential of the direct gap between the three upper valence bands and the *fourth* conduction band ($\Gamma'_{25v} \rightarrow \Gamma'_{2c}$). Fine tuning α has a rather small effect on the calculated deformation potentials. This is in line with the results reported in [53] where the enhancement of an LDA calculation with a calibrated external potential also resulted in relatively small corrections, on the order of 0.5 eV for $\Xi_d^{(\Delta)} + \Xi_u^{(\Delta)}/3 - a$ and $\Xi_d^{(L)} + \Xi_u^{(L)}/3 - a$. Compared to [53], similar trends are seen between the plain LDA values and the deformation potentials obtained after enhancing the LDA method with an additional correction. However, the calculated corrections have an even smaller magnitude here.

6.3. Effect of individual perturbative terms and of the internal displacement

Fig. 6 shows the magnitude of the effect of individual perturbative terms on the deformation potential as well as the dependence of the shear strain energy shift at the conduction L-point ($\Xi_u^{(L)}$) on the assumed internal displacement parameter ζ. The LDA potential has a comparatively weak effect on the deformation potential compared to kinetic effects or to the electrostatic potential of the nuclei (the perturbation theoretical approach is

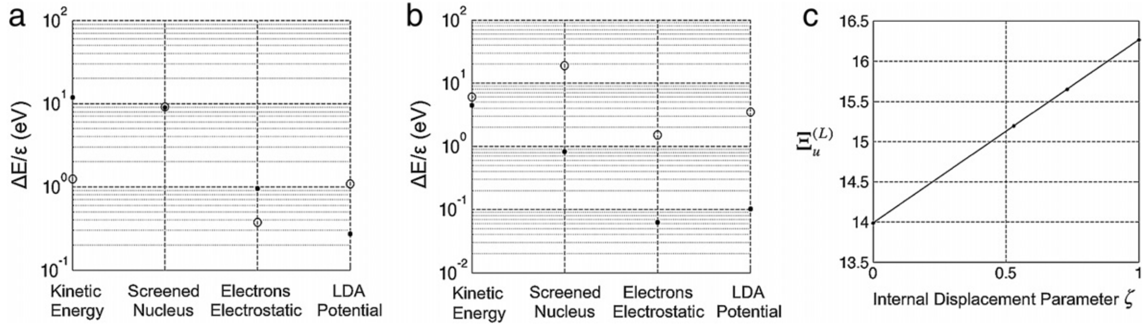

Fig. 6. Decomposition of the deformation potentials into their individual perturbative terms. (a) shows the decompositions of $\Xi_d^{(\Delta)} + \Xi_u^{(\Delta)}/3 - a$ (solid dots) as well as $\Xi_u^{(\Delta)}$ (circles). (b) shows the decompositions of $\Xi_d^{(L)} + \Xi_u^{(L)}/3 - a$ (solid dots) as well as $\Xi_u^{(L)}$ (circles). The absolute values of the terms are shown in order to plot them on a log scale. Calculations were made with $N_t = 6$, $\alpha = 5/6$, iteration number = 5 (converged electron density function) and $\zeta = 0.53$. (c) Dependence of the calculated displacement potential $\Xi_u^{(L)}$ on the assumed internal displacement parameter ζ (calculated with $N_t = 6$, $\alpha = 5/6$, iteration number = 5).

applied to wavefunctions that have already been calculated including LDA correction, i.e., this statement only refers to the *additional* energy shift induced by strain).

Due to the transformation described in Eq. (3), the nuclei remain on the same grid points irrespectively of the internal displacement. This is important to obtain a smooth dependence on ζ, since displacements of the nuclei relative to the grid points result in numerical artifacts.

7. Calculation of photoelastic coefficients

In this section we calculate the dependence of the dielectric constant of silicon on uniaxial and shear strain from the wavefunctions obtained in the previous sections. The dielectric constant is calculated with the method first devised by Adler and Wiser [58,59], but with a modified treatment of local field corrections. These are directly derived from the self-consistently calculated electron density perturbation induced by the application of the external electric field, with the dielectric constant given by

$$\varepsilon_r - 1 = \frac{4e^2}{\varepsilon_0}\left(\frac{4}{a^3}\right) \times \frac{1}{N}\lim_{q\to 0}\sum_{n\in BZ,v,c}\frac{\left(\int \psi^*_{c,k_n+q}e^{iqx}\left(-\frac{i}{q}+V_{LF}\right)\psi_{v,k_n}d^3x\right)}{E_c(k_n+q)-E_v(k_n)} \times \left(\int \psi^*_{c,k_n+q}e^{iqx}\left(-\frac{i}{q}\right)\psi_{v,k_n}d^3x\right)^* \tag{24}$$

where E_v and E_c are respectively the energies of the valence and conduction states indexed by indices v and c, k_n is a wave-vector sampled inside the 1st Brillouin zone, N is the number of sampled k-space points and $\vec{q} = q\vec{e}_x$ is an infinitesimal vector oriented along the direction of the external E-field. V_{LF} corresponds to the self-consistently calculated electrostatic and exchange potential resulting from the redistribution of the valence electron density function caused by the externally applied electric field (local field correction). The prefactor of Eq. (24) already takes into account that each state is doubly degenerate due to electron spin, so that each valence and conduction band only needs to be accounted for once in the summation.

When applying an externally applied electric field associated with an electrostatic potential $\frac{\sin(qx)}{q}$, the perturbation of the electron density distribution and the resulting potential are calculated self-consistently as functions $\rho_{LF}(x_i)\cos(qx)$ and $V_{LF}(x_i)\cos(qx)$, where $\rho_{LF}(x_i)$ and $V_{LF}(x_i)$ both have the same periodicity as the crystal lattice. Under the influence of the externally applied electric field and the induced internal potential (including the LDA correction), the valence electron wavefunctions are then transformed to the first order as

$$\psi_{v,k_n} \to \psi_{v,k_n} + \frac{e}{2}\sum_c \frac{\int \psi^*_{c,k_n+q}e^{iqx}\left(V_{LF}-\frac{i}{q}\right)\psi_{v,k_n}d^3x}{E_c(k_n+q)-E_v(k_n)}\psi_{c,k_n+q} + \frac{e}{2}\sum_c \frac{\int \psi^*_{c,k_n-q}e^{-iqx}\left(V_{LF}+\frac{i}{q}\right)\psi_{v,k_n}d^3x}{E_c(k_n-q)-E_v(k_n)}\psi_{c,k_n-q} \tag{25}$$

The equation only takes into account mixing with conduction band states, since only these contribute to the perturbation of the electron density function given by

$$\rho \to \rho + \frac{2e}{N}Re\left(\sum_{n\in BZ,v,c}\frac{\int \psi^*_{c,k_n+q}e^{iqx}\left(V_{LF}-\frac{i}{q}\right)\psi_{v,k_n}d^3x}{E_c(k_n+q)-E_v(k_n)}\psi_{c,k_n+q}\psi^*_{v,k_n} + \sum_{n\in BZ,v,c}\frac{\int \psi^*_{c,k_n-q}e^{-iqx}\left(V_{LF}+\frac{i}{q}\right)\psi_{v,k_n}d^3x}{E_c(k_n-q)-E_v(k_n)}\psi_{c,k_n-q}\psi^*_{v,k_n}\right). \tag{26}$$

where the prefactor again takes into account the dual degeneracy of the electron spin. Using $\int \psi^*_{c,k_n}\psi_{v,k_n}d^3x = 0$ we make the transformation $\frac{1}{q}\lim_{q\to 0}\int \psi^*_{c,k_n+q}e^{iqx}\psi_{v,k_n}d^3x = \frac{\partial}{\partial q}_{|q=0}\int \psi^*_{c,k_n+q}e^{iqx}\psi_{v,k_n}d^3x$. For vanishing q, Eq. (26) can then be recast into

$$\rho \to \rho + \frac{4e}{N}Re\left(\sum_{n\in BZ,v,c}\left(\frac{\int \psi^*_{c,k_n}V_{LF}\psi_{v,k_n}d^3x}{E_c(k_n)-E_v(k_n)} - i\frac{\partial}{\partial q}_{|q=0}\frac{\int \psi^*_{c,k_n+q}e^{iqx}\psi_{v,k_n}d^3x}{E_c(k_n)-E_v(k_n)}\right)\psi_{c,k_n}\psi^*_{v,k_n}\right)\cos(qx) = \rho + \rho_{LF}\cos(qx) \tag{27}$$

validating the initial assumption on the functional form of the induced valence electrons redistribution. The first term of Eq. (27) corresponds to the reaction of the electron density function to the internal field, while the second term is the reaction of the electron density function to the external field. The perturbation of the electron density function $\rho_{LF}\cos(qx)$ in turn results in the local field potential $V_{LF}\cos(qx)$ as calculated with the methods described in the previous sections (based on Eq. (20) and an adapted version of Eq. (22)). In order to calculate the photoelastic coefficients of silicon, the local field potential is self-consistently calculated for both unstrained and uniaxially strained silicon.

In a material with a cubic symmetry, the general expression of the photoelastic tensor $\delta\left(\frac{1}{\varepsilon_{ij}}\right) = p_{ijkl}\epsilon_{kl} \approx -\frac{1}{\varepsilon_0^2}\delta\varepsilon_{ij}$ reduces to [56,60,61]

$$-\frac{1}{\varepsilon_0^2}\delta\begin{pmatrix}\varepsilon_{xx}\\ \varepsilon_{yy}\\ \varepsilon_{zz}\\ \varepsilon_{xy}\\ \varepsilon_{yz}\\ \varepsilon_{zx}\end{pmatrix} = \begin{bmatrix} p_{11} & p_{12} & p_{12} & 0 & 0 & 0\\ p_{12} & p_{11} & p_{12} & 0 & 0 & 0\\ p_{12} & p_{12} & p_{11} & 0 & 0 & 0\\ 0 & 0 & 0 & p_{44} & 0 & 0\\ 0 & 0 & 0 & 0 & p_{44} & 0\\ 0 & 0 & 0 & 0 & 0 & p_{44}\end{bmatrix} \times \begin{pmatrix}\epsilon_{xx}\\ \epsilon_{yy}\\ \epsilon_{zz}\\ \epsilon_{xy}+\epsilon_{yx}\\ \epsilon_{yz}+\epsilon_{zy}\\ \epsilon_{zx}+\epsilon_{xz}\end{pmatrix}. \tag{28}$$

A number of corrective factors have to be applied to Eq. (24) when it is evaluated in the transformed coordinates used in this paper. Indeed, in the transformed coordinates the volume of the unit cell remains a^3, even though the physical volume under uniaxial strain is $(1+\epsilon)\,a^3$. In addition, a physical E-field of magnitude E results in an E-field of magnitude $(1+\epsilon)\,E$ in the transformed coordinate system when it is oriented along the uniaxial strain axis, since $-\partial V/\partial x = -(1+\epsilon_{xx})\,\partial V/\partial x'$. Similarly, under shear strain ϵ_{xy} the physical E-field $E\left(\vec{e}_x+\vec{e}_y\right)$ results in $(1+\epsilon)\,E\left(\vec{e}_x+\vec{e}_y\right)$ in the transformed coordinate system.

Under uniaxial strain Eq. (24) becomes

$$\begin{aligned}\varepsilon_r - 1 &= \frac{16e^2}{\varepsilon_0 a^3}\frac{1}{(1+\epsilon)} \times \frac{1}{N}\lim_{q\to 0}\sum_{n\in BZ,v,c}\frac{\left(\int \psi^*_{c,k_n+q}e^{iqx}\left(V_{LF}-\frac{i}{q}\right)\psi_{v,k_n}d^3x\right)}{E_c\left(k_n+q\right)-E_v\left(k_n\right)} \times\left(\int \psi^*_{c,k_n+q}e^{iqx}\left(-\frac{i}{q}\right)\psi_{v,k_n}d^3x\right)^* &(29)\\ &\simeq -\epsilon\left(\varepsilon_r-1\right)+\frac{16e^2}{\varepsilon_0 a^3} \times \frac{1}{N}\lim_{q\to 0}\sum_{n\in BZ,v,c}\frac{\left(\int \psi^*_{c,k_n+q}e^{iqx}\left(V_{LF}-\frac{i}{q}\right)\psi_{v,k_n}d^3x\right)}{E_c\left(k_n+q\right)-E_v\left(k_n\right)} \times\left(\int \psi^*_{c,k_n+q}e^{iqx}\left(-\frac{i}{q}\right)\psi_{v,k_n}d^3x\right)^* &(30)\end{aligned}$$

when the E-field is oriented along a different axis than the uniaxial strain and

$$\begin{aligned}\varepsilon_r - 1 &= \frac{16e^2}{\varepsilon_0 a^3}\frac{1}{(1+\epsilon)} \times \frac{1}{N}\lim_{q\to 0}\sum_{n\in BZ,v,c}\frac{\left(\int \psi^*_{c,k_n+q}e^{iqx}\left(V_{LF}-\frac{i}{q}\right)(1+\epsilon)\,\psi_{v,k_n}d^3x\right)}{E_c\left(k_n+q\right)-E_v\left(k_n\right)} \times\left(\int \psi^*_{c,k_n+q}e^{iqx}\left(-\frac{i}{q}\right)(1+\epsilon)\,\psi_{v,k_n}d^3x\right)^* &(31)\\ &\simeq \epsilon\left(\varepsilon_r-1\right)+\frac{16e^2}{\varepsilon_0 a^3} \times \frac{1}{N}\lim_{q\to 0}\sum_{n\in BZ,v,c}\frac{\left(\int \psi^*_{c,k_n+q}e^{iqx}\left(V_{LF}-\frac{i}{q}\right)\psi_{v,k_n}d^3x\right)}{E_c\left(k_n+q\right)-E_v\left(k_n\right)} \times\left(\int \psi^*_{c,k_n+q}e^{iqx}\left(-\frac{i}{q}\right)\psi_{v,k_n}d^3x\right)^* &(32)\end{aligned}$$

when the E-field is oriented along the same axis as the uniaxial strain. In both Eqs. (29) and (31) the factor $1+\epsilon$ in the denominator takes into account the increased volume of the unit cell. In Eq. (31) the additional factor $(1+\epsilon)^2$ in the numerator takes into account that both the external field and the internal field are effectively $1+\epsilon$ stronger in the deformed cell described in the transformed coordinate system when the uniaxial strain and the external field are along the same axis.

In order to calculate p_{44} we calculate $\varepsilon_{xx}+\varepsilon_{yy}+2\varepsilon_{xy}$ as

$$\varepsilon_{xx}+\varepsilon_{yy}+2\varepsilon_{xy}-1 = \frac{16e^2}{\varepsilon_0 a^3}\frac{1}{N}\lim_{q\to 0}\sum_{n\in BZ,v,c} \times\frac{\left(\int \psi^*_{c,k_n+q}e^{iq(x+y)}\left(V_{LF,x}+V_{LF,y}-\frac{i}{q}\right)\psi_{v,k_n}d^3x\right)}{E_c\left(k_n+q\right)-E_v\left(k_n\right)} \times\left(\int \psi^*_{c,k_n+q}e^{iq(x+y)}\left(-\frac{i}{q}\right)\psi_{v,k_n}d^3x\right)^* \tag{33}$$

where $V_{LF,x}$ and $V_{LF,y}$ are respectively the local field potentials generated by a unit external E-field oriented along the x- and y-axes. After applying a shear strain ϵ_{xy} Eq. (33) becomes

$$\begin{aligned}\varepsilon_{xx}+\varepsilon_{yy}+2\varepsilon_{xy}-1 &= \frac{16e^2}{\varepsilon_0 a^3}\frac{1}{N}\lim_{q\to 0}\sum_{n\in BZ,v,c} \times\frac{\left(\int \psi^*_{c,k_n+q}e^{iq(x+y)}\left(V_{LF,x}+V_{LF,y}-\frac{i}{q}\right)(1+\epsilon)\,\psi_{v,k_n}d^3x\right)}{E_c\left(k_n+q\right)-E_v\left(k_n\right)} \times\left(\int \psi^*_{c,k_n+q}e^{iq(x+y)}\left(-\frac{i}{q}\right)(1+\epsilon)\,\psi_{v,k_n}d^3x\right)^* &(34)\\ &\simeq 2\epsilon\left(\varepsilon_r-1\right)+\frac{16e^2}{\varepsilon_0 a^3}\frac{1}{N}\lim_{q\to 0}\sum_{n\in BZ,v,c} \times\frac{\left(\int \psi^*_{c,k_n+q}e^{iq(x+y)}\left(V_{LF,x}+V_{LF,y}-\frac{i}{q}\right)\psi_{v,k_n}d^3x\right)}{E_c\left(k_n+q\right)-E_v\left(k_n\right)} \times\left(\int \psi^*_{c,k_n+q}e^{iq(x+y)}\left(-\frac{i}{q}\right)\psi_{v,k_n}d^3x\right)^* &(35)\end{aligned}$$

in the transformed coordinate system.

Since Eqs. (30), (32) and (35) are evaluated with the wavefunctions of the strained lattice, care has to be taken to correctly normalize the wavefunctions as $\int \psi^*\psi d^3x = 1$ following either Eq. (18) or Eq. (19) depending on whether they are expressed in the physical or the transformed coordinate system.

The overall flow of the computation is summarized in Fig. 4(b). We evaluate Eqs. (24) and (29)–(34) with $q = 0.01\cdot 2\pi/a$, $\zeta = 0.53$ and $\alpha = 5/6$ for all the bands. As previously, the 1st Brillouin zone was effectively sampled with 424 k-space points spaced by $\Delta k = 0.4\pi/a$. Summations were taken over the four valence bands corresponding to outer shell electrons and the first 30 conduction bands. Due to the non-uniform grid, the eigenproblem leading to the wavefunctions is slightly non-hermitian and the wavefunctions not perfectly orthogonal to each other, leading to numerical errors increasing with the number of conduction bands taken into account in the summations. These numerical errors were alleviated by orthogonalizing the wavefunctions prior to the dielectric constant calculations, leading to a satisfactory convergence of the calculated dielectric constants (the value calculated with inclusion of 10 conduction bands is within 0.005 of the value calculated with 30 conduction bands).

The calculated dielectric constant of silicon is 13.1 prior to local field corrections and 12.4 after local field corrections. Both the calculated dielectric constant and the magnitude of the local field corrections are in line with prior LDA based calculations in the absence of additional refinements such as a scissor operator [62–64]. Table 2 summarizes the results for the photoelastic coefficients and

Table 2
Comparison of calculated photoelastic coefficients with literature values.

Coefficient	Calculated value	Lit. experimental	Lit. theory
p_{11}	-0.100[a], -0.096[b]	-0.094 ± 0.005[c]	-0.100[d], -0.097[e]
p_{12}	0.024[a], 0.020[b]	0.017 ± 0.001[c]	0.019[d], 0.015[e]
p_{44}	-0.048[a], -0.044[b]	-0.051 ± 0.002[c]	-0.050[d], -0.051[e]

[a] Calculated with ϵ $(\varepsilon_r - 1)$ evaluated with calculated ε_r.
[b] Calculated with ϵ $(\varepsilon_r - 1)$ evaluated with experimental ε_r.
[c] Measured in [65] at 0.37 eV.
[d] Calculated in [56] with DFT+LDA.
[e] Calculated in [60].

compares them to literature values. In all three Eqs. (30), (32) and (35) the first term in ϵ $(\varepsilon_r - 1)$ can be evaluated either with the calculated or experimental dielectric constant. Both results are reported in the table with a better consistency with experimental values found, as expected, in the latter case.

8. Conclusion

We have developed a real-space eigensolver based on finite differences and a non-uniform grid for solving the wavefunctions and the band diagram of strained silicon with an all-electron potential. The numerical methods are validated by comparison of the calculated bandgaps, deformation potentials, dielectric constant and photoelastic coefficients with experiment and prior modeling results. Strain was handled by a curvilinear transformation including a treatment of internal displacement. The computational method is highly flexible and is intended to be adaptable to more general classes of problems.

References

[1] T. Ghani, M. Armstrong, C. Auth, M. Bost, P. Charvat, G. Glass, T. Hoffmann, K. Johnson, C. Kenyon, J. Klaus, B. McIntyre, K. Mistry, A. Murthy, J. Sandford, M. Silberstein, S. Sivakumar, P. Smith, K. Zawadski, S. Thompson, M. Bohr, A 90 nm high volume manufacturing logic technology featuring novel 45 nm gate length strained silicon CMOS transistors, in: Electron. Devices Meeting 2003 Technical Digest, 2003, pp. 11.6.1–11.6.3.

[2] P.J.A. Thijs, L.F. Tiemeijer, P.I. Kuindersma, J.J.M. Binsma, T.V. Dongen, High-performance 1.5 μm wavelength InGaAs-InGaAsP strained quantum well lasers and amplifiers, IEEE J. Sel. Top. Quantum Electron. 27 (1991) 1426–1439.

[3] G. Masini, G. Capellini, J. Witzens, C. Gunn, High-speed, monolithic CMOS receivers at 1550 nm with Ge on Si waveguide photodetectors, in: Proc. of the 20th annual meeting of the IEEE Lasers and Electro Optics Society (LEOS), 2007, pp. 848–849.

[4] R.S. Jacobsen, K.N. Andersen, P.I. Borel, J. Fage-Pedersen, L.H. Frandsen, O. Handsen, M. Kristensen, A.V. Lavrinenko, G. Moulin, H. Ou, C. Peucheret, B. Zsigri, A. Bjarklev, Strained silicon as a new electro-optic material, Nature 441 (2006) 199–202.

[5] M. Cazzanelli, F. Bianco, E. Borga, G. Pucker, M. Ghulinyan, E. Degoli, E. Luppi, V. Véniard, S. Ossicini, D. Modotto, S. Wabnitz, R. Pierobon, L. Pavesi, Second-harmonic generation in silicon waveguides strained by silicon nitride, Nature Mater. 11 (2012) 148–154.

[6] J. Liu, X. Sun, D. Pan, X. Wang, L.C. Kimerling, T.L. Koch, J. Michel, Tensile-strained, n-type Ge as a gain medium for monolithic laser integration on Si, Opt. Express 15 (2007) 11272–11277.

[7] M. Virgillo, C.L. Manganelli, G. Grosso, T. Schroeder, G. Capellini, Photoluminescence, recombination rate, and gain spectra in optically excited n-type and tensile strained germanium layers, J. Appl. Phys. 114 (2013) 243102. 1–11.

[8] R. Geiger, M.J. Süess, R.A. Minamisawa, C. Bonzon, G. Schiefler, J. Frigerio, D. Chrastina, G. Isella, R. Spolenak, J. Faist, H. Sigg, Enhanced light emission from Ge micro bridges uniaxially strained beyond 3%, in: Proc. IEEE Conf. on Group IV Photonics (GFP), Seoul, Korea, 28–30 Aug. 2013, pp. 93-94.

[9] S. Wirths, A.T. Tiedemann, Z. Ikonic, P. Harrison, B. Holländer, T. Stoica, G. Mussler, M. Myronov, J.M. Hartmann, D. Grützmacher, D. Buca, S. Mantl, Band engineering and growth of tensile strained Ge/(Si)GeSn heterostructures for tunnel field effect transistors, Appl. Phys. Lett. 102 (2013) 192103. 1–4.

[10] W. Kohn, L.J. Sham, Self-consistent equations including exchange and correlation effects, Phys. Rev. 140 (1965) A1133–A1138.

[11] R. Gómez-Abal, X. Li, M. Scheffler, C. Ambrosch-Draxl, Influence of the core-valence interaction and the pseudopotential approximation on the electron self-energy in semiconductors, Phys. Rev.Lett. 101 (2008) 106404. 1–4.

[12] X.-Z. Li, R. Gómez-Abal, H. Jiang, C. Ambrosch-Draxl, M. Scheffler, Impact of widely used approximations to the G_0W_0 method: an all-electron perspective, New J. Phys. 14 (2012) 023006. 1–12.

[13] S. Kümmel, L. Kronik, Orbital-dependent density functionals: theory and applications, Rev. Modern Phys. 80 (2008) 3–60.

[14] A. Ormeci, H. Rosner, F.R. Wagner, M. Kohout, Y. Grin, Electron localization function in full-potential representation for crystalline materials, J. Phys. Chem. A 110 (2006) 1100–1105.

[15] S.-H. Wei, A. Zunger, Calculated natural band offsets of all II–VI and III–V semiconductors: chemical trends and the role of cation d orbitals, Appl. Phys. Lett. 72 (1998) 2011–2013.

[16] Y.-H. Li, X.G. Gong, S.-H. Wei, *Ab initio* all-electron calculation of absolute volume deformation potentials of IV–IV, III–V, and II–VI semiconductors: the chemical trends, Phys. Rev. B 73 (2006) 245206. 1–3.

[17] T.L. Beck, Real-space mesh techniques in density-functional theory, Rev. Modern Phys. 72 (2000) 1041–1080.

[18] L. Lehtovaara, V. Havu, M. Puska, All-electron density functional theory and time-dependent density functional theory with high-order finite elements, J. Chem. Phys. 131 (2009) 054103. 1–10.

[19] T.D. Engeness, T.A. Arias, Multiresolution analysis for efficient, high precision all-electron density-functional calculations, Phys. Rev. B 65 (2002) 165106. 1–10.

[20] Y. Joly, Finite-difference method for the calculation of low-energy-electron diffraction, Phys. Rev. Lett. 68 (1992) 950–953.

[21] O. Cohen, L. Kronik, A. Brandt, Locally refined multigrid solution of the all-electron Kohn–Sham equation, J. Chem. Theory. Comput. 9 (2013) 4744–4760.

[22] F. Gygi, G. Galli, Real-space adaptive-coordinate electronic-structure calculations, Phys. Rev. B 52 (1995) R2229–R2232.

[23] N.A. Modine, G. Zumbach, E. Kaxiras, Adaptive-coordinate real-space electronic-structure calculations for atoms, molecules and solides, Phys. Rev. B 55 (1997) 10289–10301.

[24] T. Ono, K. Hirose, Timesaving double-grid method for real-space electronic-structure calculations, Phys. Rev. Lett. 82 (1999) 5016–5019.

[25] S.P. Benham, J.M. Thissen, J.E. Inglesfield, self-consistent finite-difference electronic structure calculations, Comput. Phys. Comm. 136 (2001) 64–76.

[26] G.E. Pikus, G.L. Bir, Fiz. Tverd. Tela 1 (1959) 1642; English Transl: Effect of deformation on the hole energy spectrum of germanium and silicon, Sov. Phys.-Solid State 1 (1960) 1502.

[27] L.R. Saravia, D. Brust, Strain-split energy bands in semiconductors: Ge, Phys. Rev. 178 (1969) 1240–1243.

[28] L. Kleinman, Deformation potentials in silicon, I. Uniaxial strain, Phys. Rev. 128 (1962) 2614.

[29] J.C. Slater, A simplification of the Hartree–Fock method, Phys. Rev. 81 (1951) 385–390.

[30] I.N. Yakovkin, P.A. Dowben, The problem of the band gap in LDA calculations, Surf. Rev. Lett. 14 (2007) 481–487.

[31] P. Hohenberg, W. Kohn, Inhomogeneous electron gas, Phys. Rev. 136 (1964) B864–B871.

[32] O.H. Nielson, R.M. Martin, Stresses in semiconductors: ab initio calculations on Si, Ge, and GaAs, Phys. Rev. B 32 (1985) 3792–3805.

[33] The first eight eigensolutions are computed in approximately 20 s on a Mac Book Pro with a 2 GHz Intel Core i7 and 1333 MHz DDR3 memory using Matlab's eigensolver for sparse matrices (eigs). With 16 GB of memory (including the operating system), 7 eigensolvers can be run in parallel with an average completion time of 56 s for each parallel eigensolve (including the overhead from the task distribution). More intensive calculations for determining the photoelastic coefficients were run on a server with an AMD Opteron^{TM} 6380 Processor.

[34] Y. Saad, Numerical Methods for Large Eigenvalue Problems, revised edition, Society for Industrial and Applied Mathematics, ISBN: 1611970725, 2011.

[35] J.R. Chelikowsky, M.L. Cohen, Electronic structure of silicon, Phys. Rev. B 10 (1974) 5095–5107.

[36] D.M. Ceperley, B.J. Alder, Ground state of the electron gas by a stochastic method, Phys. Rev. Lett. 45 (1980) 566–569.

[37] W. Bludau, A. Onton, W. Heinke, Temperature dependence of the band gap of silicon, J. Appl. Phys. 45 (1974) 1846–1848.

[38] D.E. Aspnes, A.A. Studna, Direct observation of the E_0 and $E_0 + \Delta_0$ transitions in silicon, Solid State Commun. 11 (1972) 1375–1378.

[39] O.F. Sankey, D.J. Niklewski, Ab initio multicenter tight-binding model for molecular-dynamics simulations and other applications in covalent systems, Phys. Rev. B 40 (1989) 3979–3995.

[40] A.P. Horsfield, Efficient ab initio tight binding, Phys. Rev. B 56 (1997) 6594–6602.

[41] Y.M. Niquet, C. Delerue, G. Allan, M. Lannoo, Method for tight-binding parametrization: application to silicon nanostructures, Phys. Rev. B 62 (2000) 5109–5116.
[42] H.G. Bekker, C.M.J. Wijers, N.E. Christensen, Confinement and the CLOPW method, Physica B 217 (1996) 193–206.
[43] I. Balslev, Influence of uniaxial stress on the indirect absorption edge in silicon and germanium, Phys. Rev. 143 (1966) 636–647.
[44] K. Murase, K. Enjouji, E. Otsuka, Determination of the deformation potential constants from the electron cyclotron resonance in germanium and silicon, J. Phys. Soc. Japan 29 (1970) 1248–1257.
[45] L.D. Laude, F.H. Pollak, M. Cardona, Effects of uniaxial stress on the indirect exciton spectrum of silicon, Phys. Rev. B 3 (1971) 2623–2636.
[46] V.J. Tekippe, H.R. Chandrasekhar, P. Hisher, A.K. Ramdas, Determination of the deformation-potential constant of the conduction band of silicon from the piezospectroscopy of donors, Phys. Rev. B 6 (1972) 2348–2357.
[47] J.-C. Merle, M. Capizzi, P. Fiorini, Uniaxially stressed silicon: fine structure of the exciton and deformation potentials, Phys. Rev. B 17 (1978) 4821–4834.
[48] O. Madelung, Landolt-Börnstein (Eds.), Physics of group IV elements and III–V compounds, in: Numerical Data and Functional Relationships in Science and Technology, Group III, vol. 17a, Springer-Verlag, Berlin, 1982.
[49] C.G. Van de Walle, R.M. Martin, Theoretical calculations of heterojunction discontinuities in the Si/Ge system, Phys. Rev. B 34 (1986) 5621–5634.
[50] P. Friedel, M.S. Hybertsen, M. Schlüter, Local empirical pseudopotential approach to the optical properties of Si/Ge superlattices, Phys. Rev. B 39 (1989) 7974–7977.
[51] M.M. Rieger, P. Vogl, Electronic-band parameters in strained $Si_{1-x}Ge_x$ alloys on $Si_{1-y}Ge_y$ substrates, Phys. Rev. B 48 (1993) 14276–14287.
[52] M.V. Fischetti, S.E. Laux, Band structure, deformation potentials, and carrier mobility in strained Si, Ge, and SiGe alloys, J. Appl. Phys. 80 (1996) 2234–2252.
[53] S.-H. Wei, A. Zunger, Predicted band-gap pressure coefficients of all diamond and zinc-blende semiconductors: chemical trends, Phys. Rev. B 60 (1999) 5404–5411.
[54] C. Tserbak, H.M. Polatoglou, G. Theodorou, Unified approach to the electronic structure of strained Si/Ge superlattices, Phys. Rev. B 47 (1993) 7104–7124.
[55] G. Grosso, C. Piermarocchi, Tight-bindning model and interactions scaling laws for silicon and germanium, Phys. Rev. B 51 (1995) 16772–16777.
[56] Z.H. Levine, H. Zhong, S. Wei, D.C. Allan, J.W. Wilkins, Strained silicon: a dielectric-response calculation, Phys. Rev. B 45 (1992) 4131–4140.
[57] C.S.G. Cousins, L. Gerward, J. Staun Olsen, B. Selsmark, B.J. Sheldon, Surface effects in uniaxially stressed crystals: the internal-strain parameters of silicon and germanium revised, J. Phys. C: Solid State Phys. 20 (1987) 29–37.
[58] S.L. Adler, Quantum theory of the dielectric constant in real solids, Phys. Rev. 2 (1962) 413–420.
[59] N. Wiser, Dielectric constant with local field effects included, Phys. Rev. 1 (1963) 62–69.
[60] P. Djemia, Kh. Bouamama, *Ab-initio* calculations of the photoelastic constants of the cubic SiC polytype, J. Phys.: Conf. Ser. 454 (2013) 012060. 1–8.
[61] M. Huang, Stress effects on the peformance of optical waveguides, Internat. J. Solids Struct. 40 (2003) 1615–1632.
[62] S. Baroni, R. Resta, *Ab initio* calculation of the macroscopic dielectric constant of silicon, Phys. Rev. B 33 (1986) 7017–7021.
[63] M.S. Hybertsen, S.G. Louie, *Ab initio* static dielectric matrices from the density-functional approach, I. Formulation and application to semiconductors and insulators, Phys. Rev. B 35 (1987) 5585–5601.
[64] Z.H. Levine, D.C. Allan, Quasiparticle calculation of the dielectric response of silicon and germanium, Phys. Rev. B 43 (1991) 4187–4207.
[65] D.K. Biegelsen, Photoelastic tensor of silicon and the volume dependence of the average gap, Phys. Rev. Lett. 32 (1974) 1196–1199.